ACS NANO

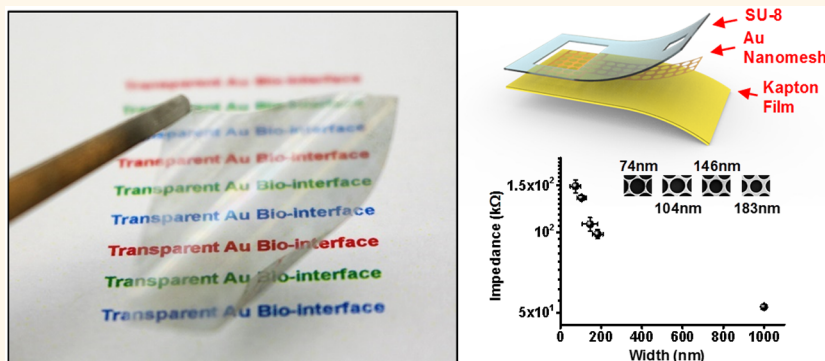# Transparent Electrophysiology Microelectrodes and Interconnects from Metal Nanomesh

Kyung Jin Seo,[†,⊥] Yi Qiang,[†,⊥] Ismail Bilgin,[‡] Swastik Kar,[‡] Claudio Vinegoni,[§] Ralph Weissleder,[§] and Hui Fang[*,†]

[†]Department of Electrical and Computer Engineering and [‡]Department of Physics, Northeastern University, Boston, Massachusetts 02115, United States

[§]Center for Systems Biology, Massachusetts General Hospital and Harvard Medical School, Boston, Massachusetts 02114, United States

Ⓢ Supporting Information

ABSTRACT: Mapping biocurrents at both microsecond and single-cell resolution requires the combination of optical imaging with innovative electrophysiological sensing techniques. Here, we present transparent electrophysiology electrodes and interconnects made of gold (Au) nanomesh on flexible substrates to achieve such measurements. Compared to previously demonstrated indium tin oxide (ITO) and graphene electrodes, the ones from Au nanomesh possess superior properties including low electrical impedance, high transparency, good cell viability, and superb flexibility. Specifically, we demonstrated a 15 nm thick Au nanomesh electrode with 8.14 $\Omega \cdot cm^2$ normalized impedance, >65% average transmittance over a 300−1100 nm window, and stability up to 300 bending cycles. Systematic sheet resistance measurements, electrochemical impedance studies, optical characterization, mechanical bending tests, and cell studies highlight the capabilities of the Au nanomesh as a transparent electrophysiology electrode and interconnect material. Together, these results demonstrate applicability of using nanomesh under biological conditions and broad applications in biology and medicine.

KEYWORDS: transparent microelectrodes, electrophysiology, cells, flexible, nanomesh, nanosphere lithography

M apping electrical activity is critical in neuroscience, cardiac physiology, and muscle contraction, among others. The stakes are perhaps the highest in the brain mapping initiative, where it is critical to measure fast currents from neurons, while simultaneously imaging the cell morphology. However, there are currently no tools that can provide both millisecond and single-cell resolutions at large scale.[1] Recently, there has been a growing interest in developing transparent microelectrodes to overcome the limitations of individual electrical and optical modalities.[2−12] By making the electrodes transparent, one can combine both optical and electrical measurements, enabling both high spatial and

temporal resolutions. These types of multimodal recordings have been extensively adopted in noninvasive neuroimaging field, such as electroencephalogram (EEG)/magnetic resonance imaging (MRI), positron emission tomography (PET)/computed tomography (CT), and MRI/magnetoencephalography (MEG), albeit at much lower resolutions.[13−16] Combining different neuroimaging modalities not only provides cross-validation measurements from different sources
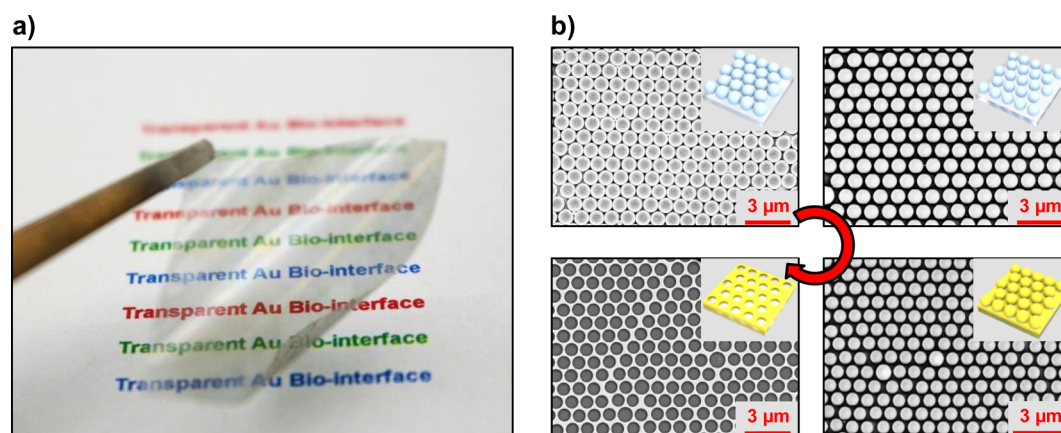
Figure 1. Au nanomesh fabrication process. (a) Image of a 15 nm thick Au nanomesh on a 15 μm thick parylene film, showing transparency and flexibility. (b) SEM images and the schematic fabrication process as insets of deposition of polystyrene nanospheres (top left), size reduction with O$_2$/CHF$_3$ RIE (top right), deposition of Cr/Au (bottom right), and lift-off (bottom left).

but also improves the spatiotemporal resolution compared to either modality alone. Similarly, measurements of neural activity and connectivity should benefit from combining fast recording from microelectrodes with optical recording/ manipulation methods, which can be used to target or identify specific neural populations in transgenic animals expressing fluorescent exogenous proteins or in recently developed optogenetics models.

Various transparent electrophysiology electrodes have been developed so far,[2−6] including indium tin oxide (ITO) and graphene, to enable concurrently electrical and optical brain mapping. ITO has excellent transparency, but its brittleness restricts the usage on irregular surfaces of the brain along with its limitation of scarcity.[17] Graphene is highly compliant; however, its cytotoxicity makes its long-term use problematic.[18] Conducting polymers also demonstrate promising conductivity, but their biocompatibility and processability are often poor.[19] Unlike these materials, metal nanomesh offers high conductivity, excellent flexibility, along with >80% transmittance over a large optical window.[20−24] In principle, nanomeshes utilizing metals such as Au, Pt, or Mo are long-term biocompatible.[21,23] Moreover, their compatibility as contacts and interconnects with active elements makes them suitable to scale up for large-area, high-density neural interfaces. Different metal nanomeshes or nanostructures have already been utilized for solar cell and other applications,[25−30] yet their electrochemical impedance properties and electrode sensing performances as electrophysiology electrodes remain largely unexplored.

In this paper, we present transparent and flexible Au nanomesh electrodes suitable for electrophysiology recordings made from nanosphere lithography and microfabrication methods. Nanosphere lithography, a widely used technique for nanostructure fabrication, allows one to tune nanomesh properties, such as transmittance and sheet resistance, by simply changing the sphere sizes, reactive ion etching (RIE) time, and thicknesses of the deposited metal.[31] We demonstrated electrodes of over 70% transmittance at 550 nm with 8.14 Ω·cm^2 normalized impedance, which corresponds to 127.2 kΩ at an 80 × 80 μm^2 electrode size. Detailed electrochemical impedance measurements further revealed that a double-layer capacitive component dominates the electrode impedance. Mechanical bending tests also showed high flexibility and robustness of the electrodes without a significant change in the

performance. Cell studies validated the cell viability of the nanomesh transparent electrodes. Together, our results demonstrate an electrode material which combines low impedance, high transmittance, great mechanical flexibility, and cell viability with important applications in both neuroscience and translational engineering.

RESULTS AND DISCUSSION

A traditional nanosphere lithography method generated the Au nanomesh film. Figure 1a shows an image of a transparent 15 nm thick Au nanomesh film on a 15 μm thick parylene substrate, which demonstrates excellent transparency and flexibility. The size of the nanomesh is 2.5 cm × 4 cm. Figure 1b illustrates scanning electron microscope (SEM) images of each fabrication step, with corresponding schematic diagrams as insets. First, we deposited polystyrene (PS) nanospheres on a surface, such as glass or a flexible substrate (Figure 1b, top left). Many PS deposition techniques exist, including an air/water interface with self-assembly,[32] dip-drawing,[33] spin-coating,[34] and unidirectional rubbing.[35] We adopted the air/water interface with a self-assembly method as it is easy to scale up, cost-effective, and applicable to any substrate.[20,32] The SEM images show highly uniform hexagonal close-packing resulting from the self-assembly method. A reactive ion etching (RIE) with CHF$_3$/O$_2$ gases further reduced the PS nanosphere sizes (Figure 1b, top right), followed by the Au deposition (Figure 1b, bottom right) and lift off (Figure 1b, bottom left). Nanomesh transmittance and sheet resistance are adjustable in the fabrication by tuning RIE conditions and depositing metals of different thicknesses, which will affect the width and thickness of Au nanomesh, respectively. Also, enabled by the versatility of nanosphere lithography, one can deposit any other metal in this process, for instance, to change other properties, such as the work function of the conductor. Sufficient RIE time and metal thickness appear to be critical, or the lines between nanospheres will disconnect, resulting in poor conductivity. For our case, width below 50 nm and/or thickness below 15 nm caused disconnection problems, significantly lowering the conductivity. Detailed fabrication procedures appear in the Methods section. This fabrication can easily scale to a larger or smaller size, suitable for applications in nearly any animal models or in human.

The electrical and optical properties of the Au nanomesh appear in Figure 2. We examined the resistance and
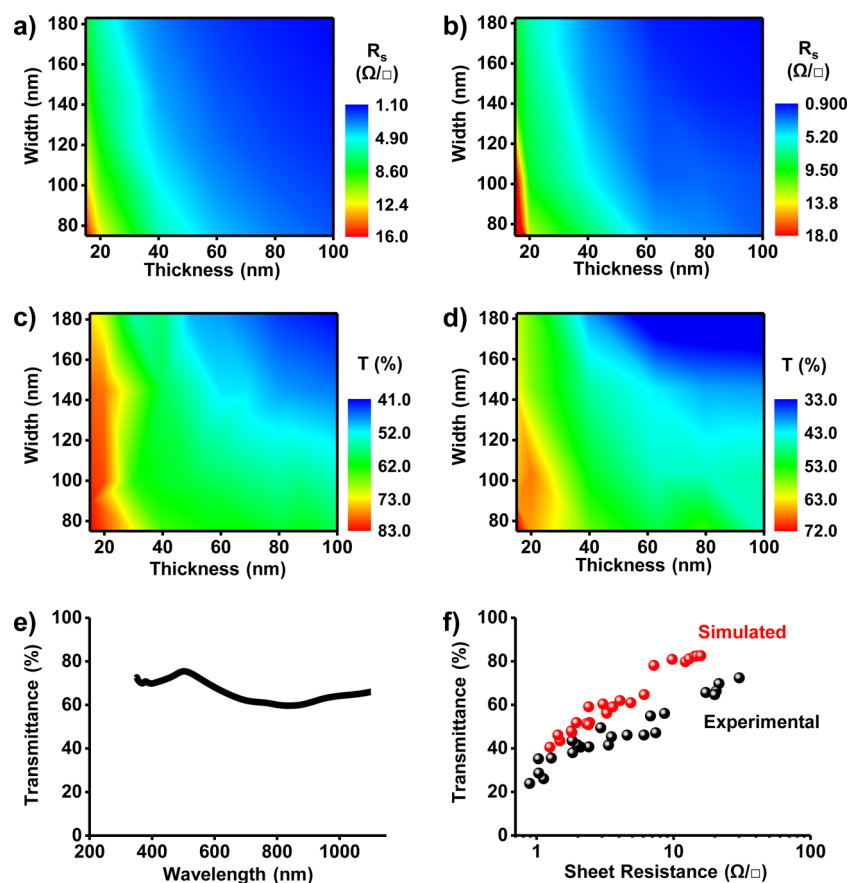
Figure 2. Sheet resistance and optical transmittance of Au nanomesh. Sheet resistance contour map of Au nanomesh of different Au thicknesses and widths with (a) simulated data and (b) experimental data. Transmittance contour map of Au nanomesh of different Au thicknesses and widths with (c) simulated data and (d) experimental data. (e) Transmittance spectrum of a Au nanomesh with width = 74 nm and thickness =15 nm. (f) Transmittance *versus* sheet resistance graph with simulated and experimental data.

transmittance of Au nanomesh with different dimensions, namely, metal thicknesses and widths. Figure 2a,b illustrates simulated and experimental sheet resistance contour maps, respectively. As the mesh thickness or width increases, the sheet resistance decreases due to increased conducting pathways for electrons to flow. Figure 2c,d plots simulated and experimental transmittance contour maps, respectively. At the same time, the transmittance also decreases due to increased area to block the light. For both properties, maps in simulated and experimental results show similar trends. The small discrepancies between simulation and experiments come from defects in the nanomesh, which emerged during the PS assembly and transfer. While it is hard to obtain a perfect hexagonal close-packing, we still achieved great transmittance over the entire sample. Compared to the no/low transmittance from thin Au films (Figure S1), the Au nanomesh demonstrates moderate–high transmittance all throughout the 300−1100 nm optical window with an average transmittance of 65% (Figures 2e and S2). High transmittance in this broad range offers great opportunities for many optical methods, such as calcium imaging, two-photon microscopy, near-infrared fluorescence imaging, and optogenetics applications.[36−39] Figure 2f summarizes transmittance values as a function of sheet resistance from both simulation and experiments, with well-matched trend—high sheet resistance results in high transmittance.

Figure 3 depicts the electrochemical impedance (EIS) characterization. The schematic diagram of the device structure appears in Figure 3a, which consists of a Kapton film (flexible

substrate), Au nanomesh electrodes, and interconnects and a SU-8 top layer for encapsulation. Detailed fabrication steps are in the Methods section. EIS measurements revealed the performance of Au nanomesh electrodes of various sizes, 20 × 20, 40 × 40, 80 × 80, and 100 × 100 μm^2, with frequencies ranging from 1 Hz to 1000 kHz. The interconnect lines are 100 μm wide for all cases. The interconnect line from Au nanomesh demonstrates 7880 Ω/cm at 10 μm line width, much smaller than graphene and ITO (Figure S3). This low resistance indicates that these nanomesh lines are suitable as high-performance interconnects for transparent electrodes. Before EIS measurements, all samples underwent UV/ozone (UVO$_3$) cleaning to remove any organic residues for better electrode contact surfaces. Figure 3b illustrates the magnitude and phase response of the impedance as measured from a sample with 15 nm thickness and 70 nm width; these conditions resulted in samples with the best transmittance in this work. This sample has the impedance of 156.6 kΩ and the phase angle of −74.5°, both at 1 kHz. This value is well within 600 kΩ, which is suitable for electrophysiology measurements.[5] The phase response of Au nanomesh shows that it is capacitive at low frequencies and resistive at high frequencies. The impedance also becomes more capacitive with increased thicknesses (Figure S4). This observation is consistent with the properties of pure Au films.[4] An equivalent circuit model fitted the EIS data, including a constant phase element (C_{PE}) in parallel with faradaic charge transfer resistance (R_{CT}) and Warburg element for diffusion (Z_W). A line resistance in series with other
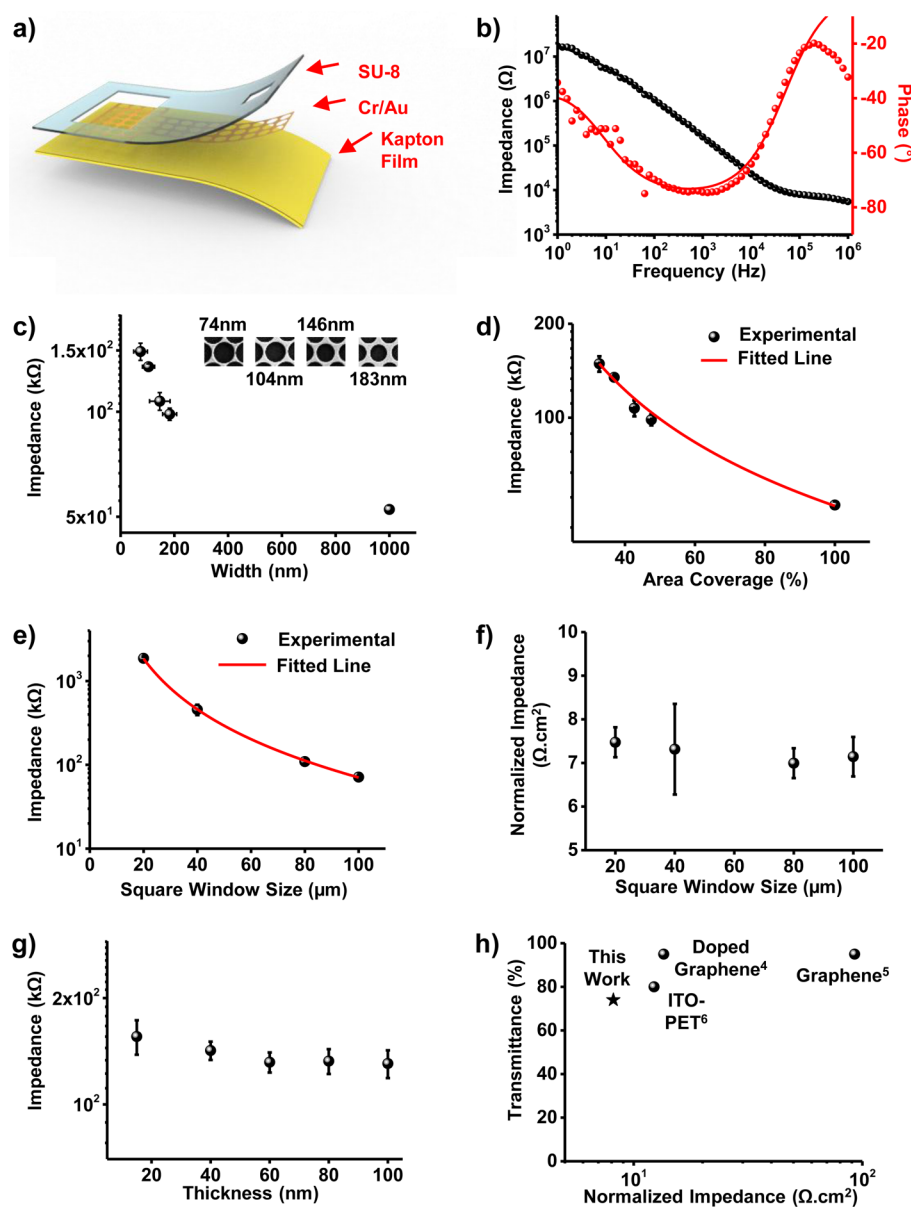
C

Figure 3. Electrochemical impedance measurements of Au nanomesh electrodes. (a) Schematic diagram of a Au nanomesh electrode with Kapton (25 μm), Cr/Au (15 nm), and SU-8 (4.5 μm) films. (b) Impedance and phase spectra of the nanomesh with width = 74 nm, thickness = 15 nm, and window size = 80 × 80 μm^2. (c) Impedance *versus* width of the nanomesh with thickness = 40 nm and window size = 80 × 80 μm^2. (d) Impedance as a function of area coverage in percentage with thickness = 40 nm and window size = 80 × 80 μm^2. (e) Impedance and square window size relationship with width = 146 nm and thickness = 40 nm. (f) Normalized impedance and square window size with width = 146 nm and thickness = 40 nm. (g) Impedance *versus* thickness with width = 74 nm and window size = 80 × 80 μm^2. (h) Transmittance as a function of normalized impedance for different TCEs.

elements modeled the resistance (R_S) of phosphate-buffered saline (PBS) solution (Figure S5). The fitted line shows a good agreement with the experimental data. Figure 3c–g depicts the relationship between the electrode impedance and parameters including metal widths, electrode window sizes, and metal thicknesses. The inset of Figure 3c shows SEM images of different widths, and a 1000 nm width indicates a complete film instead of a nanomesh. Here, we used the impedance at 1 kHz as a benchmark for electrode impedance analysis and the data collected from 40 nm thick samples as representative values. Based on the previous observation that the capacitive impedance is dominating at low frequencies, the Au nanomesh impedance mainly depends on its reactance part, which can be simplified to $1/j\omega C$, where ω is the angular frequency and C is

the double-layer capacitance in the electrode/electrolyte system. Thus, one can expect an inverse proportional relationship between impedance and surface area at low frequencies as the capacitance relates to the surface area as $\varepsilon_{dl}A/d$, where ε_{dl} and d are the permittivity and thickness of the double layer, respectively, and A is the surface area of the nanomesh. Indeed, the impedance follows a precise $1/A$ trend compared to the fitted line, in Figure 3d, which converts the metal width to area coverage (surface area in percentage) of Au nanomesh. Similarly, Figure 3e demonstrates an accurate $1/A$ trend of the 1 kHz impedance *versus* the contact area of nanomesh electrodes. The product of the 1 kHz impedance and the actual metal contact area (*i.e.*, normalized impedance) is therefore constant theoretically due to the dominating
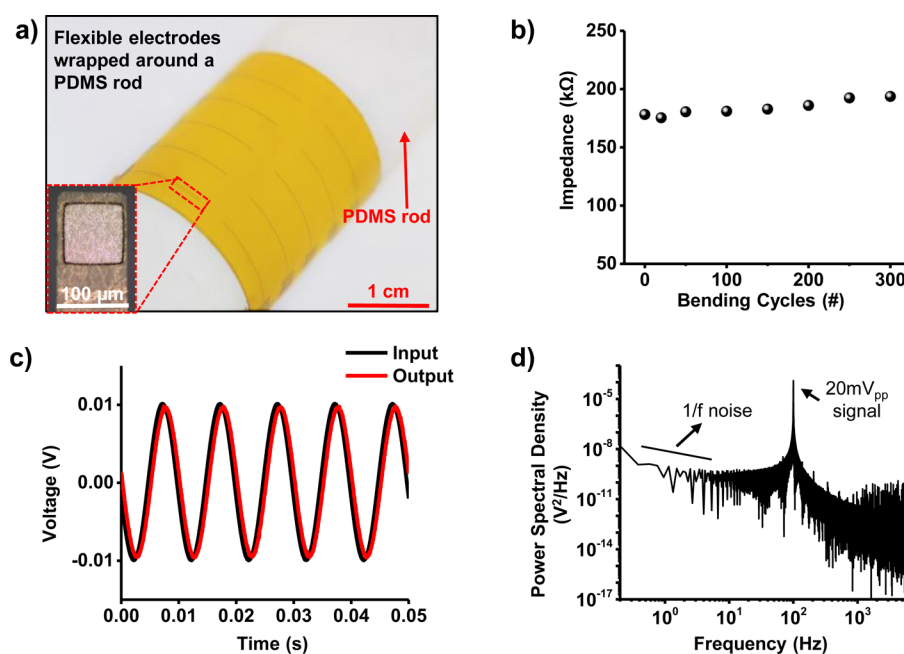
Figure 4. Mechanical bending performance and electrical bench recording from Au nanomesh electrodes. (a) Au nanomesh electrodes bent around a 9 mm radius PDMS rod. The inset shows an $80 \times 80\ \mu m^2$ window size. The Au electrode used has dimensions of width = 74 nm, thickness = 15 nm, and window size = $80 \times 80\ \mu m^2$ for b−d. (b) Bending test to a 4 mm bending radius, showing minimal impedance change. (c) Electrical bench recording output sine wave response from input sine wave (20 mV peak to peak) in aqueous PBS solution at room temperature. (d) Power spectral density of 20 mV sine wave signal at 100 Hz.

capacitance, consistent with experimental observations, as shown in Figure 3f. On the other hand, thickness of the Au nanomesh did not have a big impact on the 1 kHz impedance (Figure 3g). This phenomenon is also because the impedance is dominated by its reactance part, which originates from the double-layer capacitance at low frequencies, while thickness only changes the DC resistance of Au film. The phase angle of electrodes at 1 kHz only changed from −80 to −76° when thickness decreased by 85 nm (100 to 15 nm). This minor change proves that the increase of resistance, when reducing the metal thickness, has limited influence on the impedance because the resistance changes more than six times, while the impedance has a minimal change from 131 to 156 kΩ (19% increase). Figure 3h shows the performance comparison of Au nanomesh electrodes with several other transparent electrophysiology electrodes from ITO and graphene. Compared to previous works,[4−6] our results demonstrate 2−10 times lower impedance while possessing comparably high transmittance. This low impedance will potentially result in much less noise during electrophysiology recording. Another advantage of using a metal instead of a semimetal or semiconductor is that there is no photogenerated carriers in metal nanomesh, even at deep UV regions. This photoinertness will lead to minimal light-induced artifacts during electrophysiology recording.

One of the other compelling properties of Au nanomesh electrodes and interconnects is their great mechanical flexibility. To test the mechanical properties and sensing performance of Au nanomesh electrodes, we performed a bending test and recording from a signal function generator. We fabricated electrodes on flexible substrates to conduct the bending test. Electrodes fabricated on Kapton films were bent up to 300 cycles with a bending radius of 4 mm. Figure 4a illustrates the bent devices wrapped around a polydimethylsiloxane (PDMS) rod, showing the good flexibility of nanomesh electrodes and interconnects. The inset magnifies one electrode with an $80 \times$

$80\ \mu m^2$ square window. We characterized the flexibility and robustness of electrodes by analyzing the impedance change during the bending. After 300 bending cycles, we observed almost no impedance change, which proves a stable device performance after mechanical stressing.

We further demonstrated the recording capability of the Au nanomesh electrodes with bench testing. Figure 4c indicates an accurate response of a sine wave input signal (100 Hz, 20 mV_{pp}) recorded from Au nanomesh electrodes. We filtered the data with a 0.1 Hz to 5 kHz band-pass filter and several notch filters to remove the 60 Hz noise (hum noise) and some of its harmonics. After filtering, the output signal has a signal-to-noise ratio (SNR) of 38.2 dB, with a root-mean-square (rms) noise level of ~87 μV. The noise level can be further decreased by reducing the environmental noise and improving the data acquisition configurations. The power spectrum density (PSD) of an output signal shown in Figure 4d demonstrates detailed signal and noise information in the frequency domain. The giant peak at 100 Hz frequency came from the input signal. The noises, reflecting as small peaks in the PSD, include thermal noise, Flicker noise ($1/f$ noise), Brownian noise ($1/f^2$ noise), 60 Hz noise, and its harmonics, etc. Those noises with various frequency dependence will have different impacts at different frequency domains. The noise power density at low frequencies is usually simplified to $1/f^\alpha$, where α ranges from 0 to 2 (usually close to 1) depending on the noise components. Here, α calculated from the slope of the power density at low frequencies is about 0.87, which indicates the $1/f$ noise (flicker noise, $\alpha = 1$) is dominating at low frequencies. Thermal noise (Johnson noise), which is another important noise source, will significantly decrease with lowering impedance due to its noise mechanism. Under thermal equilibrium, the PSD of the noise in an electrode/electrolyte system would be $4kTZ_r(\omega)$ ($Z_r(\omega)$ representing the real part of impedance, and kT is the thermal energy)[40] dictated by the Johnson−Nyquist formulation of
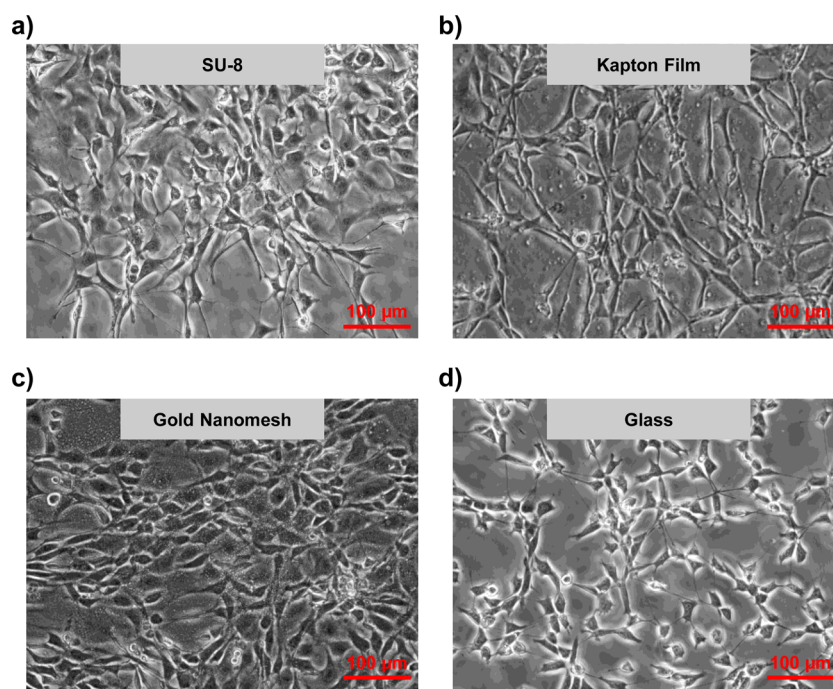
Figure 5. Cell studies on Au nanomesh. Phase contrast images of 3T3 mouse embryonic fibroblast cells grown on the device's different substrates after 7 days: (a) SU-8, (b) Kapton, (c) Au nanomesh, and (d) glass coverslip.

thermal noise.[41,42] Thus, smaller impedance would naturally result in a lower noise level. The PSD becomes independent of the frequency at higher frequencies since $Z_r(\omega)$ mainly comes from a constant series resistance (R_S),[40] reflecting that the white noise $(\alpha = 0)$ is dominating in this region. The low noise level due to the better electrode impedance demonstrates the significant advantage of Au nanomesh electrodes in suppressing electrical interference noises. In addition to metal nanomesh, we also envision that other metallic nanostructures, such as electrospun nanotrough and nanowire crosses, may also be used here if metal structures are dense enough (with spacings less than a few microns) and uniformly distributed.[28,29]

To test cell viability and cell adhesion on as-grown films, we incubated 3T3 mouse embryonic fibroblast cells on separate microscope coverslips where the three different films constituting the three separate layers of the device structure (SU-8, Kapton, Au nanomesh) were grown. Additionally, we also incubated cells on a coverslip covered with a thin film of Au and on a control coverslip for comparison. Figure 5 shows cells growing on all films maintained a viability similar to the control after 7 days, indicating that the nanomesh substrates do not have any adverse effects on the cell viability and are highly promising for future *in vitro* and *in vivo* studies (see also Figure S6 for cell study results of thin gold film and gold nanomesh in a zoomed-in area).

CONCLUSIONS

In conclusion, we have successfully demonstrated transparent electrophysiology microelectrodes and interconnects from flexible Au nanomesh using nanosphere lithography and microfabrication techniques. From electrical/optical/mechanical characterization and cell studies, Au nanomesh demonstrated high conductivity, great flexibility, good transmittance, and cell viability. Detailed EIS measurements and bench testing revealed that Au nanomesh electrodes have remarkably low impedance, making them suitable as high-performance trans-

parent electrophysiology electrodes. Future studies will focus on developing large-scale passive and active arrays from metal nanomesh electrodes and interconnects and applying them for concurrent electrical and optical brain mapping *in vivo*.

METHODS

Materials and Tools. Polystyrene nanospheres (carboxyl latex bead, 4% w/v, 1.0 μm) were purchased from Thermo Fisher Scientific. Chloroform $(CHCl_3)$ was purchased from Fisher Chemical, and PBS (Tablets) was purchased from Fisher BioReagents. All materials were used as received. SEM, 4-point probe, and a UV spectrometer characterized the packing of nanospheres, sheet resistance, and transmittance of the Au nanomesh, respectively.

Fabrication of Au Nanomesh Samples. The fabrication began with the deposition of polystyrene nanospheres (1 μm in diameter) on a 3 in. $\times$ 1 in. glass slide placed in a 4 in. plastic Petri dish with DI water. We used PS nanospheres of 1 μm in diameter to achieve a good trade-off between transmittance and conductivity of the Au nanomesh. The holes in the nanomesh should be smaller than the sizes of neurons, typically on the order of a few tens of microns, to be patternable to achieve multielectrode arrays. On the other hand, if holes are too small, much smaller than a few hundred nanometers, the nanomesh transmittance would decrease as the resulting holes are comparable to the light wavelengths that are of interest to optical measurements. We carefully adjusted the water level to be the same as the top surface of the glass slide while not immersing the glass slide fully for an air/water interface. Using carboxyl-functionalized spheres is crucial for this air/water interface technique. A 3 mL pipet then applied polystyrene nanosphere solution, mixed with equal volume of ethanol, to the glass slide, and the mixed solution slowly propagated to the edge of the glass slide. When the solution arrived at the edge and reached the water interface, the PS nanospheres dispersed along the surface of the water, making a polystyrene monolayer. Repetitions of this step led to a coverage of 90% of the Petri dish with PS nanospheres. After enough coverage was achieved, adding more water increased the water level for easier scooping, which transferred the PS nanosphere monolayers from the water surface to a host substrate, such as a glass slide or a Kapton film. We immediately dried the host substrate with the scooped monolayer at room temperature by tilting

the substrate as vertically as possible. Tilting plays an important role to prevent line defects of multiple layers formed during the drying process. Reducing the size of the nanospheres began with inductively coupled plasma (ICP) RIE using O_2 and CHF_3 gases. The conditions were 40 sccm of O_2, 2 sccm of CHF_3, 25 mT, and 100 W for radio frequency power 1 (RF_1) and 150 W for RF_2. RIE generated the plasma with an RF-powered magnetic field, which made the etching more isotropic. RF_1 represents the power from RIE, and RF_2 is the power from ICP, generating very dense plasma. Using different time or power can tune the size of PS nanospheres. CHF_3 gas helped to get more conformal etching and to etch sidewalls of the nanospheres.[43] For metal deposition, we used e-beam evaporation for an easier lift-off process. Depositions of 1 nm of Cr and 15 nm of Au were at the rates of 0.5 and 1 A/s, respectively, yielding the metal layer. For lift-off, sonication of the aforementioned samples in chloroform for 2 min resulted in the Au nanomesh on its host substrate.

Fabrication of Nanomesh Electrodes. After lift-off, a positive photoresist (S1818, Shipley) spin-coated the Au nanomesh using 3000 rpm for 30 s. Then, photolithography defined the electrode and interconnect patterns with UV exposure and development, followed by wet etching of Au and chromium layers with Au and chrome etchants, respectively. Acetone, isopropyl alcohol (IPA), and DI water removed the remaining photoresist. SU-8 2005 spin-coated the patterned nanomesh electrodes using 3000 rpm for 30 s for contact area isolation. After soft baking at 95 °C for 2 min, UV exposed the SU-8 for 7 s, followed by a postexposure baking at 95 °C for 3 min. For development, sonication in SU-8 developer for 30 s and rinsing with fresh SU-8 developer and IPA yielded clear SU-8 patterns. Hard bake at 200 °C for 20 min finalized the process. The thickness of SU-8 was 4.5 μm. The fabricated electrode had a 10 mm length, 100 μm width, and 2 mm × 3 mm contact pad size.

Electrochemical Impedance Measurement. Before measurements, we used UV/ozone (UVO_3) (Bioforce Nanosciences, Inc. Procleaner 110) to clean the samples for 20 min to have a cleaner contact surface area. Electrochemical impedance spectroscopy measurements consisted of Gamry Gamry Reference 600+ potentiostat/galvanostat/ZRA (Gamry Instruments), adopting a three-electrode configuration with 0.01 M PBS solution at room temperature. The reference electrode was Ag/AgCl, and the counter electrode was a platinum wire. The sweeping frequencies ranged from 1 Hz to 1000 kHz with a 10 mV RMS AC voltage. The circuit model used for fitting is available in the Supporting Information. We used infinite Warburg element for diffusion (Z_w) because of the best goodness of fit achieved.

Sheet Resistance and Transmittance Simulation. The finite difference time domain software (FDTD Solutions) simulated the optical properties of Au nanomesh (transmittance). The simulated model consisted of uniformly distributed 3 × 3 unit cells of Au nanomesh and used symmetric/antisymmetric conditions. Using different thicknesses and widths (diameter of holes) yielded the relationship between thickness and width. Finite element analysis simulation (COMSOL 5.2) yielded resistance of the Au nanomesh structure (Figure S7) with different thicknesses and widths created by the 3D model in COMSOL 5.2. The equation $R_S = R \times W/L$ derived sheet resistance, where W and L represent width and length of the conductor, respectively. Both optical and electrical simulation results are in good agreement with experimental data and simulated values from other literature, as well.[20]

Electrical Bench Recording. We generated a 100 Hz, 20 mV_{pp} sine wave input signal using a function generator (Agilent 33120A) with a 50 dB attenuator. By using a platinum electrode, we applied the input signal to the 0.01 M PBS solution. Meanwhile, we immersed the Au nanomesh electrode into the PBS solution for recording. PBS solution, working as transmission media here, transmitted the input signal to the Au nanomesh electrode, eventually to a data acquisition tool, NI USB-6210 (National Instruments), which is connected to the pad of the nanomesh electrode (Figure S8). The MATLAB software (Math Works) drove the data acquisition and enabled real-time signal processing, which includes filtering and SNR calculation.

Cell Culture and Imaging. 3T3 cells were incubated in culture medium in a T125 flask at 37 °C with 5% CO_2 in humidified air. When 80% confluency was reached, cells were trypsinized with a 0.5% trypsin solution. Cells were then placed in a 50 mL falcon tube, and the enzyme was deactivated by adding twice the cell culture media. The cell suspension was then centrifuged at 300g for 3 min and resuspended at approximately 50 000 cells/mL in media. The seeding film-covered coverslips and control were placed in six-well plates in triplicate, and cell suspensions were delicately placed on the surface of the coverslips. Four hours after cell plating, 2 mL of media was added and cells were incubated for 7 days (37 °C, 5% (w/v) CO_2) before imaging. Images were acquired in transmission mode through the films using an inverted microscope (Eclipse TE2000-s, Nikon) operating in phase-contrast mode for capturing cell morphology.

ASSOCIATED CONTENT

Ⓢ Supporting Information

The Supporting Information is available free of charge on the ACS Publications website at DOI: 10.1021/acsnano.7b01995.

Thin gold film properties; transmittance spectrum of a 15 nm thick Au nanomesh with different widths; resistance study of different materials; phase spectrum of 74 nm wide Au nanomesh with different thicknesses; impedance circuit model and its detailed equations; additional cell studies; simulation model for both optical and electrical properties; and photograph of electrical bench testing setup (PDF)

AUTHOR INFORMATION

Corresponding Author

*E-mail: h.fang@northeastern.edu.

ORCID 🟢

Kyung Jin Seo: 0000-0001-9743-2026

Author Contributions

⊥K.J.S. and Y.Q. contributed equally to this work. K.J.S., Y.Q., and H.F. designed the research; K.J.S. and Y.Q fabricated the devices; K.J.S., Y.Q., I.B., and S.K. performed data analysis; C.V. and R.W. carried out cell studies; K.J.S., Y.Q., C.V., and H.F. co-wrote the manuscript while all other authors provided feedback.

Notes

The authors declare no competing financial interest.

REFERENCES

(1) Sejnowski, T. J.; Churchland, P. S.; Movshon, J. A. Putting Big Data to Good Use in Neuroscience. *Nat. Neurosci.* **2014**, *17*, 1440–1441.

(2) Ledochowitsch, P.; Olivero, E.; Blanche, T.; Maharbiz, M. M. In *A Transparent μECoG Array for Simultaneous Recording and Optogenetic Stimulation*, 2011 Annual International Conference Proceedings; IEEE Eng. Med. Biol. Soc., Boston, MA, Aug. 30–Sept. 3, 2011; pp 2937–2940.

(3) Kwon, K. Y.; Sirowatka, B.; Li, W.; Weber, A. *Opto-μECoG array: Transparent μECoG Electrode Array and Integrated LEDs for Optogenetics*, 2012 IEEE Biomed. Circuits Syst. Conference (BioCAS), Hsinchu, Taiwan, 28–30 Nov. 2012; pp 164–167.

(4) Kuzum, D.; Takano, H.; Shim, E.; Reed, J. C.; Juul, H.; Richardson, A. G.; de Vries, J.; Bink, H.; Dichter, M. A.; Lucas, T. H.; Coulter, D. A.; Cubukcu, E.; Litt, B. Transparent and Flexible Low Noise Graphene Electrodes for Simultaneous Electrophysiology and Neuroimaging. *Nat. Commun.* **2014**, *5*, 5259.

(5) Park, D. W.; Schendel, A. A.; Mikael, S.; Brodnick, S. K.; Richner, T. J.; Ness, J. P.; Hayat, M. R.; Atry, F.; Frye, S. T.; Pashaie, R.; Thongpang, S.; Ma, Z.; Williams, J. C. Graphene-Based Carbon-Layered Electrode Array Technology for Neural Imaging and Optogenetic Applications. *Nat. Commun.* **2014**, *5*, 5258.

(6) Kunori, N.; Takashima, I. A Transparent Epidural Electrode Array for Use in Conjunction with Optical Imaging. *J. Neurosci. Methods* **2015**, *251*, 130−137.

(7) De, S.; Lyons, P. E.; Doherty, E. M.; Nirmalraj, P. N.; Blau, W. J.; Boland, J. J.; Coleman, J. N.; Higgins, T. M. Silver Nanowire Networks as Flexible, Transparent, Conducting Films, Extremely High DC to Optical Conductivity Ratios. *ACS Nano* **2009**, *3*, 1767−1774.

(8) Hsu, P. C.; Wang, S.; Wu, H.; Narasimhan, V. K.; Kong, D.; Ryoung Lee, H.; Cui, Y. Performance Enhancement of Metal Nanowire Transparent Conducting Electrodes by Mesoscale Metal Wires. *Nat. Commun.* **2013**, *4*, 2522.

(9) Kim, S.; Lee, J.-L. Design of Dielectric/Metal/Dielectric Transparent Electrodes for Flexible Electronics. *J. Photonics Energy* **2012**, *2*, 021215−021215.

(10) Park, H.; Brown, P. R.; Bulovic, V.; Kong, J. Graphene as Transparent Conducting Electrodes in Organic Photovoltaics: Studies in Graphene Morphology, Hole Transporting Layers, and Counter Electrodes. *Nano Lett.* **2012**, *12*, 133−140.

(11) Jo, G.; Choe, M.; Cho, C. Y.; Kim, J. H.; Park, W.; Lee, S.; Hong, W. K.; Kim, T. W.; Park, S. J.; Hong, B. H.; Kahng, Y. H.; Lee, T. Large-Scale Patterned Multi-Layer Graphene Films as Transparent Conducting Electrodes for GaN Light-Emitting Diodes. *Nanotechnology* **2010**, *21*, 175201.

(12) Kasry, A.; Kuroda, M. A.; Martyna, G. J.; Tulevski, G. S.; Bol, A. A. Chemical Doping of Large-Area Stacked Graphene Films for Use as Transparent, Conducting Electrodes. *ACS Nano* **2010**, *4*, 3839−3844.

(13) Zhang, F.; Wang, L. P.; Brauner, M.; Liewald, J. F.; Kay, K.; Watzke, N.; Wood, P. G.; Bamberg, E.; Nagel, G.; Gottschalk, A.; Deisseroth, K. Multimodal Fast Optical Interrogation of Neural Circuitry. *Nature* **2007**, *446*, 633−639.

(14) Gotman, J.; Kobayashi, E.; Bagshaw, A. P.; Benar, C.-G.; Dubeau, F. Combining EEG and fMRI A Multimodal Tool for Epilepsy Research. *J. Magn. Reson. Imaging* **2006**, *23*, 906−920.

(15) Gerth, H. U.; Juergens, K. U.; Dirksen, U.; Gerss, J.; Schober, O.; Franzius, C. Significant Benefit of Multimodal Imaging: PET/CT Compared with PET alone in Staging and Follow-up of Patients with Ewing Tumors. *J. Nucl. Med.* **2007**, *48*, 1932−1939.

(16) Dale, A. M.; Liu, A. K.; Fischl, B. R.; Buckner, R. L.; Belliveau, J. W.; Lewine, J. D.; Halgren, E. Dynamic Statistical Parametric Mapping: Combining fMRI and MEG for High-Resolution Imaging of Cortical Activity. *Neuron* **2000**, *26*, 55−67.

(17) Paetzold, R.; Heuser, K.; Henseler, D.; Roeger, S.; Wittmann, G.; Winnacker, A. Performance of Flexible Polymeric Light-Emitting Diodes under Bending Conditions. *Appl. Phys. Lett.* **2003**, *82*, 3342−3344.

(18) Zhang, Y.; Ali, S. F.; Dervishi, E.; Xu, Y.; Li, Z.; Casciano, D.; Biris, A. S. Cytotoxicity Effects of Graphene and Single-Wall Carbon Nanotubes in Neural Phaeochromocytoma-Derived PC12 Cells. *ACS Nano* **2010**, *4*, 3181−3186.

(19) Kaur, G.; Adhikari, R.; Cass, P.; Bown, M.; Gunatillake, P. Electrically Conductive Polymers and Composites for Biomedical Applications. *RSC Adv.* **2015**, *5*, 37553−37567.

(20) Gao, T.; Wang, B.; Ding, B.; Lee, J. K.; Leu, P. W. Uniform and Ordered Copper Nanomeshes by Microsphere Lithography for Transparent Electrodes. *Nano Lett.* **2014**, *14*, 2105−2110.

(21) Guo, C. F.; Sun, T.; Liu, Q.; Suo, Z.; Ren, Z. Highly Stretchable and Transparent Nanomesh Electrodes Made by Grain Boundary Lithography. *Nat. Commun.* **2014**, *5*, 3121.

(22) Kim, W. K.; Lee, S.; Hee Lee, D.; Hee Park, I.; Seong Bae, J.; Woo Lee, T.; Kim, J. Y.; Hun Park, J.; Chan Cho, Y.; Ryong Cho, C.; Jeong, S. Y. Cu Mesh for Flexible Transparent Conductive Electrodes. *Sci. Rep.* **2015**, *5*, 10715.

(23) Jang, H. Y.; Lee, S.-K.; Cho, S. H.; Ahn, J.-H.; Park, S. Fabrication of Metallic Nanomesh: Pt Nano-Mesh as a Proof of Concept for Stretchable and Transparent Electrodes. *Chem. Mater.* **2013**, *25*, 3535−3538.

(24) Zhu, J. F.; Zeng, B. Q.; Wu, Z. Enhanced Broadband Optical Transmission Through Ultrathin Metallic Nanomesh. *J. Electromagnet. Wave* **2012**, *26*, 342−352.

(25) Guo, C. F.; Liu, Q.; Wang, G.; Wang, Y.; Shi, Z.; Suo, Z.; Chu, C. W.; Ren, Z. Fatigue-free, Superstretchable, Transparent, and Biocompatible Metal Electrodes. *Proc. Natl. Acad. Sci. U. S. A.* **2015**, *112*, 12332−12337.

(26) Cheng, K.; Cui, Z.; Li, Q.; Wang, S.; Du, Z. Large-Scale Fabrication of a Continuous Gold Network for Use as a Transparent Conductive Electrode in Photo-Electronic Devices. *Nanotechnology* **2012**, *23*, 425303.

(27) Zhu, J.; Zhu, X.; Hoekstra, R.; Li, L.; Xiu, F.; Xue, M.; Zeng, B.; Wang, K. L. Metallic Nanomesh Electrodes with Controllable Optical Properties for Organic Solar Cells. *Appl. Phys. Lett.* **2012**, *100*, 143109.

(28) Wu, H.; Kong, D.; Ruan, Z.; Hsu, P. C.; Wang, S.; Yu, Z.; Carney, T. J.; Hu, L.; Fan, S.; Cui, Y. A Transparent Electrode Based on a Metal Nanotrough Network. *Nat. Nanotechnol.* **2013**, *8*, 421−425.

(29) Lee, Y.; Min, S. Y.; Kim, T. S.; Jeong, S. H.; Won, J. Y.; Kim, H.; Xu, W.; Jeong, J. K.; Lee, T. W. Versatile Metal Nanowiring Platform for Large-Scale Nano- and Opto-Electronic Devices. *Adv. Mater.* **2016**, *28*, 9109−9116.

(30) Parvathy Devi, B.; Wu, K.-C.; Pei, Z. Gold Nanomesh Induced Surface Plasmon for Photocurrent Enhancement in a Polymer Solar Cell. *Sol. Energy Mater. Sol. Cells* **2011**, *95*, 2102−2106.

(31) Haynes, C. L.; Van Duyne, R. P. Nanosphere Lithography: A Versatile Nanofabrication Tool for Studies of Size-Dependent Nanoparticle Optics. *J. Phys. Chem. B* **2001**, *105*, 5599−5611.

(32) Rybczynski, J.; Ebels, U.; Giersig, M. Large-Scale, 2D Arrays of Magnetic Nanoparticles. *Colloids Surf., A* **2003**, *219*, 1−6.

(33) Shieh, J. Y.; Kuo, J. Y.; Weng, H. P.; Yu, H. H. Preparation and Evaluation of the Bioinspired PS/PDMS Photochromic Films by the Self-Assembly Dip-Drawing Method. *Langmuir* **2013**, *29*, 667−672.

(34) Shinde, S. S.; Park, S. Oriented Colloidal-Crystal Thin Films of Polystyrene Spheres *via* Spin Coating. *J. Semicond.* **2015**, *36*, 023001.

(35) Park, C.; Lee, T.; Xia, Y.; Shin, T. J.; Myoung, J.; Jeong, U. Quick, Large-Area Assembly of a Single-Crystal Monolayer of Spherical Particles by Unidirectional Rubbing. *Adv. Mater.* **2014**, *26*, 4633−4638.

(36) Stosiek, C.; Garaschuk, O.; Holthoff, K.; Konnerth, A. *In vivo* Two-Photon Calcium Imaging of Neuronal Networks. *Proc. Natl. Acad. Sci. U. S. A.* **2003**, *100*, 7319−7324.

(37) Helmchen, F.; Fee, M. S.; Tank, D. W.; Denk, W. A Miniature Head-Mounted Two-Photon Microscope: High-Resolution Brain Imaging in Freely Moving Animals. *Neuron* **2001**, *31*, 903−912.

(38) Gioux, S.; Choi, H. S.; Frangioni, J. V. Image-Guided Surgery Using Invisible Near-Infrared Light: Fundamentals of Clinical Translation. *Mol. Imaging* **2010**, *9*, 237−255.

(39) Deisseroth, K. Optogenetics: 10 years of Microbial Opsins in Neuroscience. *Nat. Neurosci.* **2015**, *18*, 1213−1225.

(40) Rocha, P. R. F.; Schlett, P.; Kintzel, U.; Mailänder, V.; Vandamme, L. K. J.; Zeck, G.; Gomes, H. L.; Biscarini, F.; de Leeuw, D. M. Electrochemical Noise and Impedance of Au Electrode/Electrolyte Interfaces Enabling Extracellular Detection of Glioma Cell Populations. *Sci. Rep.* **2016**, *6*, 34843.

(41) Nyquist, H. Thermal Agitation of Electric Charge in Conductors. *Phys. Rev.* **1928**, *32*, 110−113.

(42) Johnson, J. B. Thermal Agitation of Electricity in Conductors. *Phys. Rev.* **1928**, *32*, 97−109.

(43) Barcelo, S. J.; Lam, S.-T.; Gibson, G. A.; Sheng, X.; Henze, D. Nanosphere Lithography Based Technique for Fabrication of Large Area, Well Ordered Metal Particle Arrays. *Proc. SPIE* **2012**, *4*, 83232L.